Proceedings of the ASME 2010 3rd Joint US-European Fluids Engineering Summer Meeting and 8th International Conference on Nanochannels, Microchannels, and Minichannels
FEDSM-ICNMM2010
August 1-5, 2010, Montreal, Canada

FEDSM-ICNMM2010-30767

THE EFFECTS OF BLOCKING RATIO AND ATMOSPHERIC ALTITUDE ON STARTING ANNULAR JETS

Emad Abdel-Raouf*, John Baker*, Muhammad Sharif†

***Department of Mechanical Engineering, The University of Alabama**
Box 870276, Tuscaloosa, AL 35487, USA.
†Department of Aerospace Engineering & Mechanics, The University of Alabama
Box 870280, Tuscaloosa, AL 35487, USA

ABSTRACT

The effects of the blocking ratio and atmospheric altitude on starting annular air jets at a low Reynolds number are investigated by examining the velocity profiles, jet entrainment and vortex formation. A 2D axisymmetric numerical model is developed to perform the analysis. The numerical model is validated with theoretical and experimental results from other studies. In order to achieve a comprehensive analysis, the annular jet is tested for blocking ratios with the values of 0.00 (i.e. a round jet), 0.50 and 0.75. Air properties at altitudes of 0.00 km, 18.90 km and 33.75 km are tested to simulate atmospheric environments at sea level, edge of near space and near space, respectively. The results showed that the starting jet velocity profile, entrainment and vortex formation is a strong function of blocking ratio. On the other hand, the same parameters are shown to be nearly independent, strong and weak functions of atmospheric altitude, respectively.

1. INTRODUCTION

A starting jet is an impetus fluid that is discharged via a nozzle or an orifice into a dormant fluid. According to Pawlak et al. (2007), starting jets are common in many applications including fuel and oxidizer jets in combustion chambers, pressured vessel breaches, tidal jets, and animal propulsion. Such class of jet problems is associated with high fluid entrainment that is enhanced by the formation of vortices. Most of the literature on this topic has been focused on studying both the jet (i.e. annular jets, round jets, etc.) structure and the vortex formation.

The investigation of the structure of starting annular jets has typically been undertaken by examining the velocity profiles and jet entrainment. It has been customary to divide the region near the jet entry into three zones: initial, intermediate, and fully developed [Ko and Lam (1985)]. Circulation takes place in the initial zone, while reattachment takes place in the intermediate zone. In the fully developed zone, the dimensionless velocity profile does not show much change at different axial positions.

The velocity profiles in the three zones have been studied extensively. For example, Uyttendaele and Shambaugh (1989) studied annular jets with sharp-edged inlets to simulate the melt blowing process for producing microfibers. They found out that the lengths of the three zones and the velocity profiles in fully developed zone are independent of the Reynolds number and the length to stroke ratio of the orifice. Ko and Chan (1978) studied annular jet for three nozzle configurations at the center: basic (i.e. no central bullet), conical bullet, and elliptical bullet. The examined configurations produced similar results within each of the three velocity profile zones.

Besides the velocity profiles, fluid entrainment has been closely considered. Kuhlman (1987) compared the far-field entrainment that resulted from annular and circular jets. He concluded that annular jet entrainment is 43% higher than circular jet entrainment under the same conditions. Hill (1972) measured the entrainment of an air jet. He found out that entrainment is independent of the Reynolds number for values greater than 60,000 and that it is highly dependent on the axial distance.

In addition to jet structure, vortex formation that is generated by starting jets has been analyzed. Morteza et al. (1998) studied the vortex formation of starting water jets through a piston and cylinder experimental setup. After experimenting with several piston velocity profiles, they found that the maximum circulation of the generated vortex rings happened

at a dimensionless time, which they called the 'formation number', in the range of 3.6 to 4.5. Yu et al. (2007) included the effects of gravity on a starting water jet issuing through a converging nozzle. Their jets were tested for three Reynolds numbers: 2358, 3528 and 4716. For the leading vortex, they noted leapfrogging in the former and pinch-off in the latter two Reynolds number cases.

In this study, the effects of blocking ratio and atmospheric altitudes on very low Reynolds number starting annular jets are investigated by analyzing the velocity profiles, jet entrainment, and vortex formation. The annular jet configuration that is used is the same as the one used by Krueger and Gharib (2003) and will be described in the following section. The blocking ratio ratios that are used are 0.00, 0.50 and 0.75, where the first represents a round jet. The atmospheric altitudes are 0.00km, 18.90km and 33.75km, corresponding to sea level, edge of near space and near space altitudes, respectively. Note that low Reynolds number flow is of particular importance because entrainment would be optimized as indirectly concluded by Wall et al. (1980), who pointed out that entrainment decreased by increasing the Reynolds number and remained constant for Reynolds number values greater than 23,000. In addition, low Reynolds number flow covers numerous biological flow applications that have been associated with vortex formation as investigated by Dabiri (2009) and Dabiri and Gharib (2005).

2. PROBLEM SPECIFICATION

The starting jet under the current study is assumed to be formed by air passing through an annular tube exiting into a quiescent ambient atmosphere. The tip angle, α, of the annular tube is 7° and the hydraulic diameter is $D = 1.27cm$. The inner and outer radii are related to the hydraulic diameter such that

$$2\left(d_{out} - d_{in}\right) = D \tag{1}$$

The blocking ratio, BR, is defined in terms of the inner and outer radii such that

$$BR = \frac{d_{in}}{d_{out}} \tag{2}$$

and is tested for the values of BR={0, 0.5, 0.75}. In addition, the length of the annular tube is

$$L = 6.125 \cdot D \tag{3}$$

In order to ensure that the flow at exit of the annular tube is fully developed, the length of the tube is assumed to be equivalent to the hydrodynamic length, which according to Incropera et al. (2007) can be expressed for laminar flow as

$$\frac{L}{D} = 0.05 \cdot \mathrm{Re} \tag{4}$$

where the Reynolds Number, Re, is

$$\mathrm{Re} = \frac{V_o \cdot D}{\upsilon} \tag{5}$$

Substituting Equation (3) into Equation (4) yields a Reynolds number of 122.5, which will be the value used throughout the analysis. Note that a starting jet with a Reynolds number of 122.5 can be correctly considered laminar, since the cutoff for turbulent flow in round jets is Re=1000, according to Boguslawski and Popiel (1979).

The analysis is carried out at the following atmospheric altitudes: sea level (0.00 km), edge of near space (18.90 km) and near space (33.75 km). The tabulated values by Sissenwine et al. (1976) for the atmospheric air properties at the specified three altitudes are used. As a result, the uniform velocity, V_o, from Equation (5) at 0.00 km, 18.90 km and 33.75 km is calculated to be 0.1409, 1.31 and 14.6 m/s, respectively. Furthermore, these uniform velocities produce Mach numbers that are well below 0.3, hence ensuring that air can be treated as an incompressible fluid in this problem.

3. NUMERICAL MODEL

The 2D axisymmetric incompressible Navier-Stokes equations in dimensionless form, as presented by Rosenfeld et al. (1998), are

$$\frac{\partial U_R}{\partial T} + U_R \frac{\partial U_R}{\partial R} + U_X \frac{\partial U_R}{\partial X} = \ldots$$
$$\ldots \frac{1}{R}\frac{\partial}{\partial R}\left(R\sigma_{RR}\right) - \frac{1}{R}\sigma_{\theta\theta} + \frac{\partial \sigma_{RX}}{\partial X} \tag{6}$$

$$\frac{\partial U_X}{\partial T} + U_R \frac{\partial U_X}{\partial R} + U_X \frac{\partial U_X}{\partial X} = \ldots$$
$$\ldots \frac{1}{R}\frac{\partial}{\partial R}\left(R\sigma_{RX}\right) + \frac{\partial \sigma_{XX}}{\partial X} \tag{7}$$

and the conservation of mass is

$$\frac{1}{R}\frac{\partial}{\partial R}\left(RU_R\right) + \frac{\partial U_X}{\partial X} = 0 \tag{8}$$

where the stress components can be expressed as

$$\sigma_{RR} = -P + \frac{2}{\mathrm{Re}}\frac{\partial U_R}{\partial R} \tag{9}$$

$$\sigma_{\theta\theta} = \frac{2}{\mathrm{Re}}\frac{\partial U_R}{\partial R} \tag{10}$$

$$\sigma_{RX} = \frac{1}{\mathrm{Re}}\left(\frac{\partial U_R}{\partial X} + \frac{\partial U_X}{\partial R}\right) \tag{11}$$

and

$$\sigma_{XX} = -P + \frac{2}{\mathrm{Re}}\frac{\partial U_X}{\partial X} \tag{12}$$

Note that Equation (6) is the momentum equation in the radial direction R, Equation (7) is the momentum equation in the axial direction X and Equation (8) is the continuity equation.

The Navier-Stokes equations, Equations (6)-(12), are solved using a commercial CFD package that utilizes a finite volume numerical method. A second order upwind discretization scheme was selected. The outer dimensions of the mesh are 50m in the radial direction and 300m in the axial direction. Figure 1 shows the outer boundaries of the mesh that was used

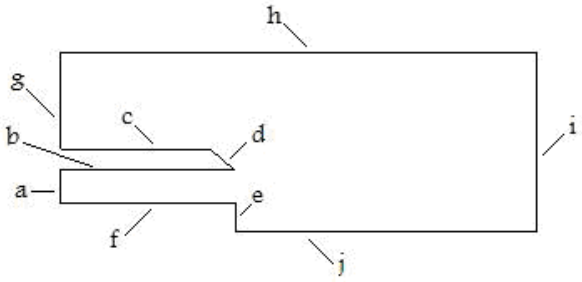

FIGURE 1. Outer Boundary of Mesh.

by the CFD package. Note that the Fig. 1 is purposely not drawn to scale in order to show the features of the annular tube. The labeled sides represent the various boundaries. Side *a* represents a velocity inlet boundary. Sides *b*-*e* represent a wall boundary condition. Side *f* represents a wall boundary for blocking ratios, BR, of 0.5 and 0.75 but represent an axial boundary condition when BR=0. Side *j* represents an axial boundary. Side *g* represents a pressure-inlet boundary, while sides *h* and *i* represent a pressure-outlet boundary.

In addition, a 69220-cell grid along with a time step of 0.00025s was used for the CFD analysis. Figure 2 shows the pressure coefficient along the axis, i.e. side *j* from Fig. 1,

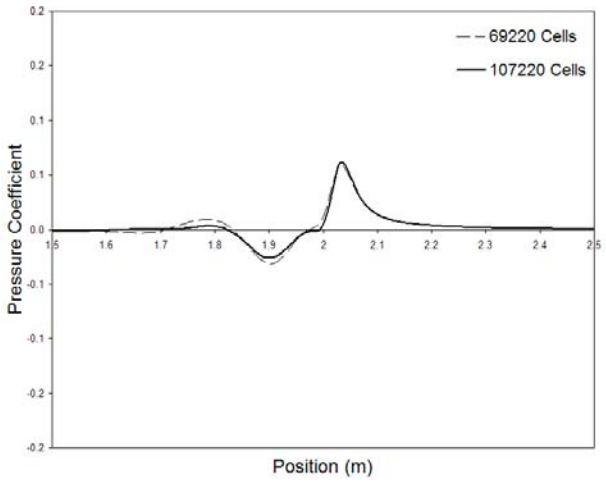

FIGURE 2. Grid spatial convergence.

generated by both a 69220-cell and 107220-cell mesh grids using a time step of 0.0005s. Since both solutions are near identical, the usage of a 69220-cell model produced a spatial independent solution. Similarly, the usage of a time step of 0.00025s produced a temporal independent solution as shown in Fig. 3, where the pressure coefficient curve at the axis was near identical for the 0.00025s and 0.0001s time steps.

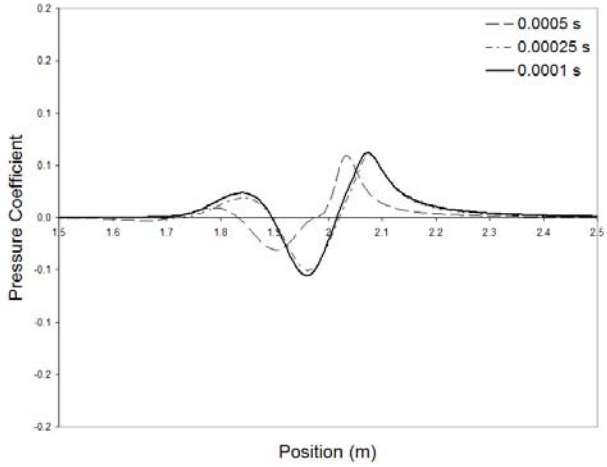

FIGURE 3. Grid time convergence.

4. VALIDATION

The theoretical and experimental equations for the dimensionless velocity profile of fully developed round jets

(i.e. BR=0) at standard atmospheric conditions respectively are

$$\frac{V}{V_m} = \left(1 + \left(2^{1/2} - 1\right)\left(\frac{r}{r_{1/2}}\right)^2\right)^{-2} \qquad (13)$$

and

$$\frac{V}{V_m} = \exp\left(-0.693 * \left(\frac{r}{r_{1/2}}\right)^2\right) \qquad (14)$$

where Equation (13) was derived by Uyttendaele and Shambaugh (1989) based on the works of Tollmien (1926) and Reichardt (1951) and Equation (14) was presented by Obot et al. (1984) based on their experiment results. Figure 4 shows a comparison between the numerical solution and the theoretical

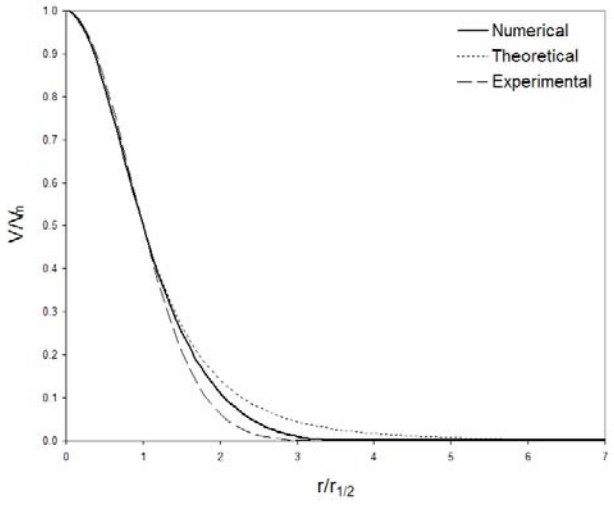

FIGURE 4. Numerical results validation.

and experimental solutions that are generated by Equations (13) and (14), respectively, at an axial position of 100 diameters away from the exit of the tube. From observation, the numerical solution is "sandwiched" between the theoretical and experimental solutions, thus indicating the validity of the numerical model.

5. RESULTS AND DISCUSSION

5.1. Velocity Profiles

The velocity profiles at a given dimensionless axial distance (x/D) are studied by plotting the dimensionless velocity (V/V_m) against the dimensionless radial distance ($r/r_{1/2}$), where $r_{1/2}$ is the half radius of the maximum velocity V_m. Figure 5a-c respectively shows the velocity profile of a round jet (i.e. zero blocking ratio) in the initial, intermediate, and fully developed zones at several axial distances. The selected axial distances, x/D, for the three zones are {0.5, 1, 2, 3}, {5, 7, 10, 15} and {25, 50, 75, 100}, respectively. As can be noted in Fig. 5, the intensity of the 'zigzag' behavior of the velocity profile is the indicator of the zone classification for a round jet. Thus, for a round jet with a low Reynolds number flow at standard atmospheric conditions, the initial zone takes place at axial distances less than 5 hydraulic diameters; the intermediate zone takes at axial distances between 5 and 15 hydraulic diameters; and the fully developed takes place at axial distances greater than 15 hydraulic diameters.

Figures 6 and 7 show the velocity profiles for blocking ratios of 0.50 and 0.75, respectively, at the same axial locations and letter grouping of Fig. 5. The velocity profiles under each subfigure of Figs. 7 and 8 exhibit similar characteristics. Hence, the span of the three zones is independent or at the very least a weak function of the blocking ratio. Furthermore, in addition to the 'zigzag' indicator of the round jets, the zone classification of jets with non-zero blocking ratio can also be characterized by the size of the multimodal shapes of the velocity profiles, as shown in Figs. 6 and 7. The initial and intermediate zones of Fig. 7 exhibit more prominent multimodal shapes than their respective zones of Fig. 6. Thus, increasing the blocking ratio increases the size of the multimodal shapes of the velocity profiles in the initial and intermediate zones. The velocity profiles in the fully developed zone, however, retain the unimodal character of the round jets as shown in Figs. 5c, 6c, and7c.

Unlike the blocking ratio, the atmospheric altitude has a very weak effect on the velocity profile for low Reynolds number fluid flow. Figure 8 shows the effect of atmospheric altitude conditions at {0.00 km, 18.90 km, 33.75 km} on the velocity profiles at x/D={0.5, 10, 50}with a uniform blocking ratio of 0.50. Note that the three axial positions represent the three zones. As observed, the velocity profiles in the three zones are essentially not affected by the atmospheric altitudes. This fact can be more clearly noted in Fig. 9, which shows the dimensionless centerline velocity decay (V_o/V_m) along the axial direction (x/D) at the various conditions. The centerline velocity decay is a strong function of the blocking ratio and a weak function of altitude.

5.2. Entrainment

Entrainment is analyzed by looking at the jet penetration, the ratio of the total mass flow to initial mass flow rates, and the spread of the jet. In this study, penetration and total mass flow rate are calculated at the tip of the jet, and thus it is convenient to track those parameters as a function of time as previously done by Witze (1980) and Joshi and Schreiber (2006). The dimensionless time, T, in this study is defined as

$$T = \frac{t \cdot V_o}{D} \qquad (15)$$

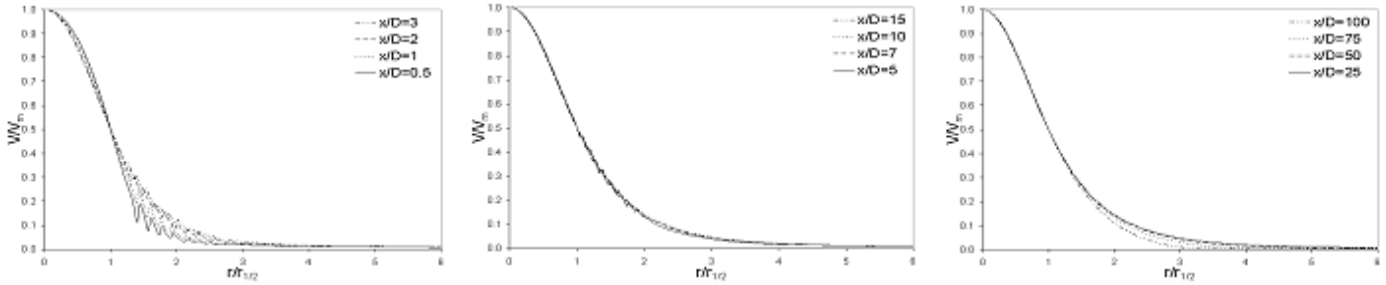

a. Initial zone b. Intermediate zone c. Fully developed zone

FIGURE 5. Velocity profiles with BR=0.00 at sea level.

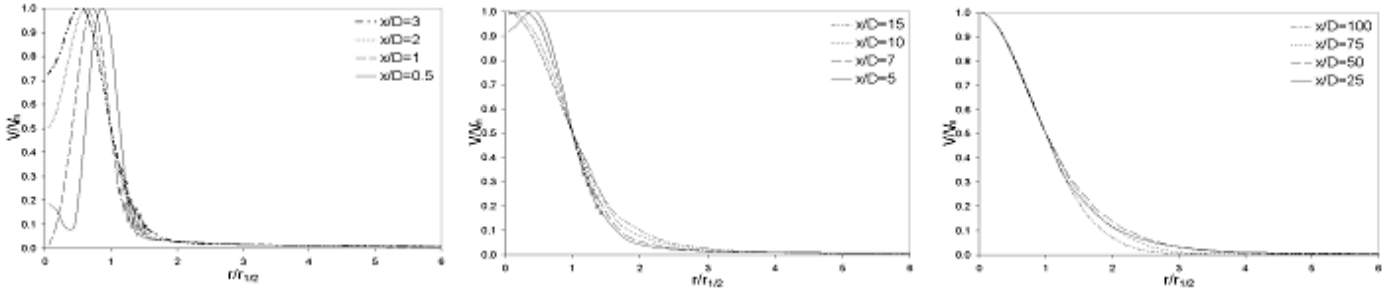

a. Initial zone b. Intermediate zone c. Fully developed zone

FIGURE 6. Velocity profiles with BR=0.50 at sea level.

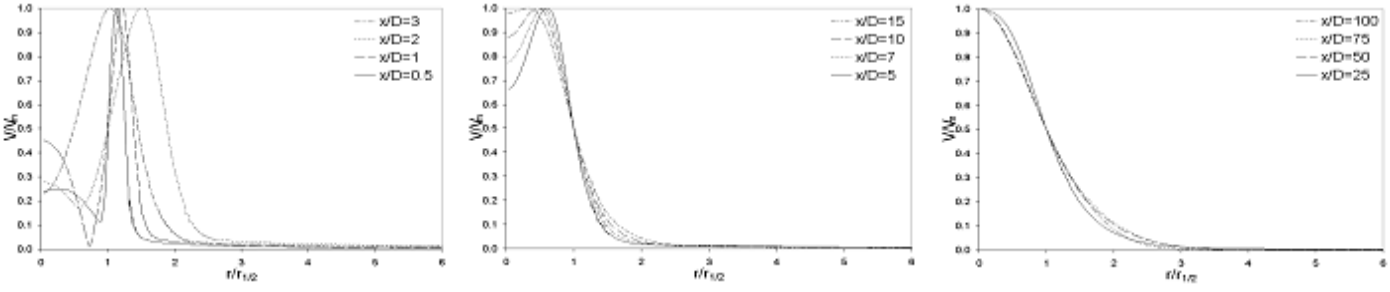

a. Initial zone b. Intermediate zone c. Fully developed zone

FIGURE 7. Velocity profiles with BR=0.75 at sea level.

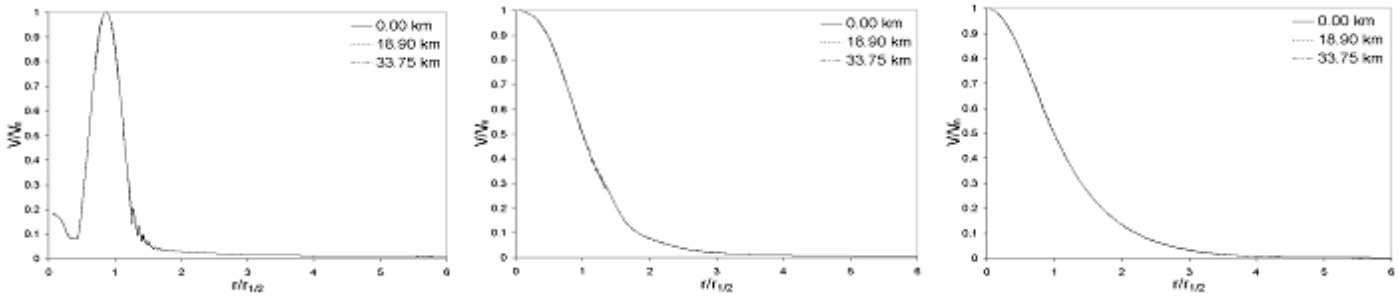

a. Initial zone (x/D=0.5) b. Intermediate zone (x/D=10) c. Fully developed zone (x/D=50)

FIGURE 8. Velocity profiles with BR=0.5 at multiple atmospheric altitudes.

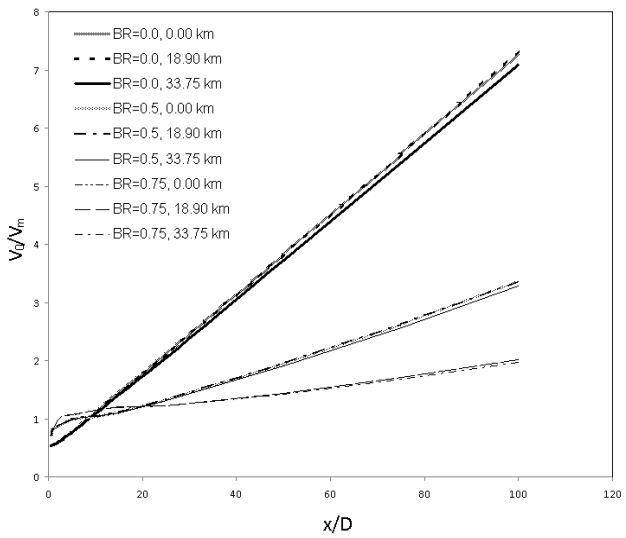

FIGURE 9. Velocity centerline decay.

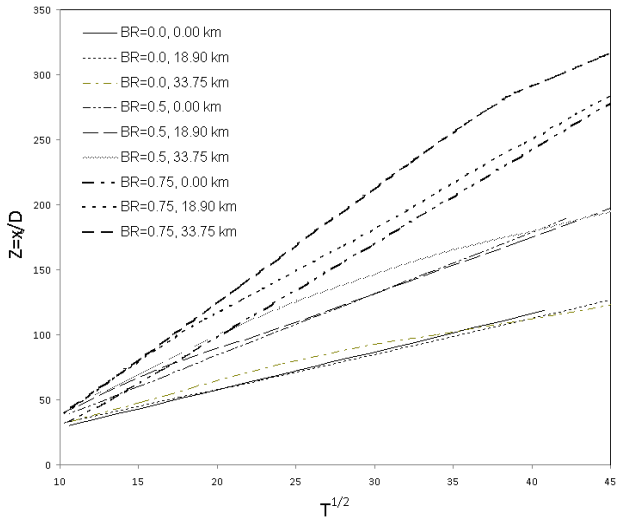

FIGURE 10. Dimensionless penetration depth of jet tip.

Figure 10 shows the dimensionless penetrations depth of the jet tip, $Z = x_t / D$, as a function of the square root of dimensionless time, $T^{1/2}$, for various blocking ratios and pressures. By examining the jet penetration curves, it becomes clear that the slope is a strong function of the blocking ratio while the linearity is a strong function of the altitude. Increasing the blocking ratio increases the slope of the penetration curves, hence increasing the penetration of the jet tip at any given time. In addition, lowering the altitude increases the linearity of the penetration curve such that it becomes a linear function of time at sea level.

Figure 11 shows the mass flow rate ratio (i.e. total mass to initial mass flow rates), M, as a function of the square root of dimensionless time, $T^{1/2}$. The mass flow ratio has a strong

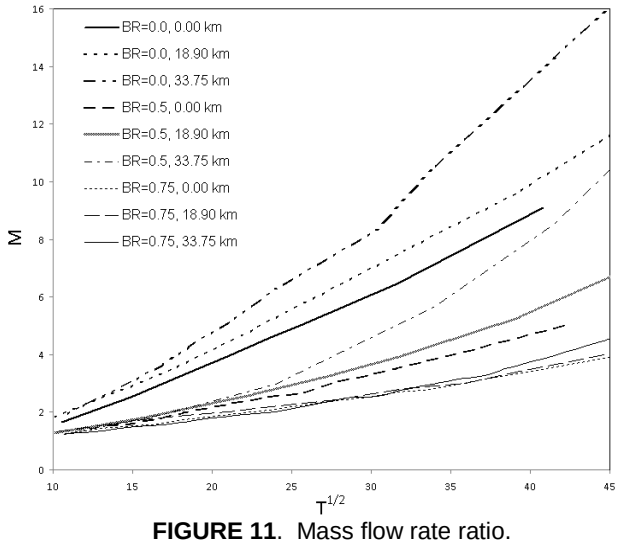

FIGURE 11. Mass flow rate ratio.

inverse relationship with the blocking ratio, as shown in Fig. 11. Decreasing the blocking ratio increases the mass flow ratio such that a round jet (i.e. BR=0) produced the highest mass flow ratio. On the other hand, higher altitudes increase the mass flow ratio but only after a lag time that increases with larger blocking ratios. The dimensionless lag times for the blocking ratios of {0.00, 0.50, 0.75} are about {13, 22, 40}, respectively. Before those lag times, the mass flow ratio is a weak function of altitude. The mass flow ratio, however, becomes a strong function of altitude after the lag time and increases by lowering the altitude, as shown in Fig. 11.

Figure 12 shows the spread of the jet under various blocking ratios and atmospheric altitudes. The spread is presented by plotting the dimensionless half radius, $r_{1/2}/D$, growth along the dimensionless axial position, x/D. It is evident from the plot that spread is a strong function of blocking ratios and a weak function of altitudes. For axial distances greater that 15 hydraulic diameters, the spread plots become linear, making it a characteristic of the fully developed zone. In the linear sections, it can be observed that the slope of the half radius growth decreases with increasing blocking ratio.

5.3. Vortex Formation

Unlike many studies [Kreuger and Gharib (2003), Rosefeld et al. (1998), Gharib et al. (1998)] that sought to optimize the velocity functions of the starting jets by using the vortex formation number as a test criteria, a major aim of this study is to examine how starting jet vortices are affected by the blocking ratio and atmospheric altitude. By setting the starting jet inlet velocity as a constant throughout the duration of the jet, the velocity function is in fact ignored and the focus is set on the generated vortices themselves. The vortices generated by the specified blocking ratio and atmospheric altitude cases are compared by their circulation and vortex

Reynolds number, for which the latter was calculated by Kreuger and Gharib (2003) by

$$\mathrm{Re}_\Gamma = \frac{\Gamma}{\nu} \tag{16}$$

where Γ is the circulation of the vortex. In this study, circulation is calculated by summing the vorticity across the surface area of a torus, which is generated by the axisymmetric model through the rotation of a circle that is created in the r-x plane. The center of the circle is the 'eye' of the vortex that is visible in the 2D plane and its radius was chosen to be in 0.004 m for all blocking ratio and altitude cases.

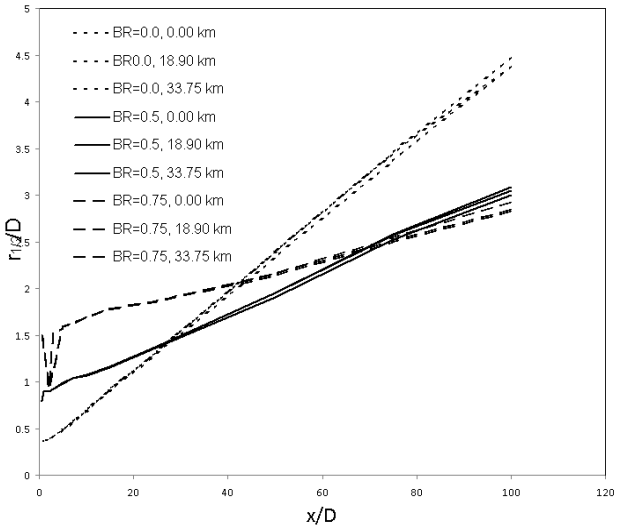

FIGURE 12. Dimensionless half radius growth (or spread).

Tables 1 and 2 show the circulation and the vortex Reynolds number, respectively, for specified blocking ratios and atmospheric altitudes at dimensionless time, T=11. From Table 1, it can be observed that circulation, Γ, is a strong function of both the blocking ratio and atmospheric altitude, since circulation increases with larger blocking ratios and at higher altitudes. However, by examining Table 2, it turns out that the vortex Reynolds number, Re_Γ, is a strong function of blocking ratio but a weak function of altitude. The fact that a certain fluid has larger circulation at higher altitudes does not mean vortex formation is a strong function of altitude due to the change of the fluid's atmospheric properties, which is accounted for by the vortex Reynolds number. Making a comparison through circulation alone would have been misleading. Altogether, vortex formulation is strong function of blocking ratio and a weak function of altitude.

Table 1. Circulation, Γ, in (m/s) at T=10.

Altitude	BR=0.00	BR=0.50	BR=0.75
0.00 km	0.0044	0.0078	0.034
18.90 km	0.032	0.089	0.34
33.75 km	0.29	0.76	3.7

Table 2. Vortex Reynolds number, Re_Γ, at T=10.

Altitude	BR=0.00	BR=0.50	BR=0.75
0.00 km	3.0×10^2	5.4×10^2	2.3×10^3
18.90 km	2.3×10^2	6.5×10^2	2.5×10^3
33.75 km	1.9×10^2	5.0×10^2	2.5×10^3

6. CONCLUSION

Starting annular air jets at a low Reynolds number of 122.5 were analyzed for blocking ratios of 0.00, 0.50 and 0.75 at atmospheric altitudes of 0.00 km, 18.90 km and 33.75 km. The results are presented in the following points.

- The initial velocity profile zone is located within 5 hydraulic diameters of the starting jet entrance; the intermediate zone is located between 5 and 15 hydraulic diameters; and the fully developed zone in located beyond 15 hydraulic diameters.
- The lengths of the velocity profile jet zones are near independent of blocking ratio and atmospheric altitude.
- The size of unimodal and multimodal velocity profile shapes in the initial and intermediate zones increase with larger blocking ratios.
- Velocity profiles in each of the three zones are a strong function of the blocking ratios and nearly independent of altitude.
- The centerline velocity decay is a strong function of the blocking ratio and a weak function of altitude. Decreasing the blocking ratio and lowering the altitude increases centerline velocity decay, reaching a maximum for BR=0.00 at 0.00 km.
- The slope of the penetration of the jet tip is a strong function of the blocking ratio such that increasing the blocking ratio makes the jet penetration slopes steeper.
- The linearity of the penetration of the jet tip is a strong function of atmospheric altitude such that lowering the altitude increases linearity. At sea level, the jet penetration is linear.

- Decreasing the blocking ratio increases the mass flow ratio of the total to initial mass rates.
- Higher altitudes increase the mass flow ratio after a lag time that increases with larger blocking ratios
- The half radius growth (or spread) is a strong function of blocking ratio and a weak function of altitude.
- The half radius growth is linear in the fully developed zone (i.e. distances greater than 15 hydraulic diameters).
- Vortex formation is a strong function of the blocking ratio and a weak function of altitude, as evident from vortex Reynolds number calculations.

ACKNOWLEDGEMENT

The authors would like to thank the U.S. Department of Education for its support through the Graduate Assistance in Areas of National Need (GAANN) Fellowship.

REFERENCES

L. Boguslawski, C.Z. Popiel, Flow structure of the free round turbulent jet in the initial region, J Fluid Mech (1979), vol 90, n 3, pp 531-539.

J. Dabiri, Optimal vortex formation as a unifying principle in biological propulsion, Annu Rev Fluid Mech (2009), vol 41, pp 17-33.

J. Dabiri, M. Gharib, The role of optimal vortex formation in biological fluid transport, Proc R Soc B (2005), vol 272, pp 1557-1560.

M. Gharib, E. Rambod, K. Shariff, A universal time scale for vortex ring formation, J Fluid Mech (1998), vol 360, pp 121-140.

B. Hill, Measurement of local entrainment rate in the initial region of axisymmetric turbulent air jets, J Fluid Mech (1972), vol 51, n 4, pp 773-779.

F. Incropera, D. Dewitt, T. Bergman, A. Lavine, Introduction to Heat Transfer, 5th Ed, John Wiley & Sons (2007), pp 457.

A. Joshi, W. Schreiber, An experimental examination of an impulsively started incompressible turbulent jet, Experiments in Fluids (2006), vol 40, pp 156-160.

N. Ko, W. Chan, Similarity in the initial region of annular jets: three configurations, J Fluid Mech (1978), vol 84, n 4, pp 641-656.

N. Ko, K. Lam, Flow structures of a basic annular jet, AIAA Journal (1985), vol 23, n 8, pp 1185-1190.

P. Krueger, M. Gharib, The significance of vortex ring formation to the impulse and thrust of a starting jet, Phys Fluids (2003), vol 15, n 5, pp 1271-1281.

J. Kulman, Variation of entrainment in annular jets, AIAA Journal (1987), vol 35, n 3, pp 373-379.

N. Obot, M. Graska, T. Trabold, The near field behavior of round jets at moderate Reynolds numbers, Can J Chem Eng (1984), vol 62, n 5, pp 587-593.

G. Pawlak, C.M. Cruz, C.M. Bazan, P.G. Hardy, Experimental characterization of starting jet dynamics, Fluid Dynamics Research (2007), vol 39, pp 711-730.

H. Reichardt, On new theory of free turbulence, Roy Aeronautical Soc — J (1943), vol 47, n 390, pp 167-176.

M. Rosenfeld, E. Rambod, M. Gharib, Circulation and formation number of laminar vortex rings, J Fluid Mech (1998), vol 376, pp 297-318.

N. Sissenwine, M. Dubin, S. Teweles, COESA Co-Chairmen, 1976: U.S. Standard Atmosphere, 1976. Stock No. 003-017-00323-0, U.S. Government Printing Office, Washington, D.C. USA.

W. Tollmien, Berechnung turbulenter ausbreitungsvorgange, Z Angew Math Mech (1926), vol 6, n 6, pp 468-478.

M. Uyttendaele, R. Shambaugh, The flow of annular jets at moderate Reynolds numbers, Ind Eng Chem Res (1989), vol 28, pp 1735-1740.

T. Wall, H. Nguyen, V. Subramanian, T. Mai-Viet, P. Howley, Direct measurements of the entrainment by single and double concentric jets in the regions of transition and flow establishment, Trans IChemE (1980), vol 58, pp 237-241.

P. Witze, The impulsively started incompressible turbulent jet, Sandia Laboratories report (1980), SAND80-8617.

S. Yu, A. Law and J. Ai, Vortex formation process in gravity-driven starting jets, Exp Fluids (2007), vol 42, pp 783-797.

NOMENCLATURE

BR	blocking ratio
d	annular tube radius (m)
D	hydraulic diameter (m)
L	length of annular tube (m)
M	mass flow rate ratio of total to initial values
P	dimensionless pressure
r	radial coordinate (m)
R	dimensionless radial coordinate
Re	Reynolds number
t	time (s)
T	dimensionless time
U	dimensionless velocity
V	velocity (m/s)
x	axial coordinate (m)
X	dimensionless axial coordinate
Z	dimensionless jet tip penetration
α	tip angle of annular tube
Γ	vortex circulation (m^2/s)
ν	kinematic viscosity (m^2/s)
σ	dimensionless shear stress

Subscript

m	maximum value
o	initial value
R	radial direction
t	jet tip
X	axial direction
Γ	vortex value
θ	transverse direction